Surface-Enhanced Raman Spectroscopy of Graphene

Fred Schedin,[†] Elefterios Lidorikis,[‡] Antonio Lombardo,[§] Vasyl G. Kravets,[†] Andre K. Geim,[†] Alexander N. Grigorenko,[†] Kostya S. Novoselov,[†,*] and Andrea C. Ferrari[§,*]

[†]Department of Physics and Astronomy, Manchester University, Manchester, U.K., [‡]Department of Materials Science and Engineering, University of Ioannina, Ioannina, Greece, and [§]Department of Engineering, University of Cambridge, Cambridge CB3 0FA, U.K.

ABSTRACT Surface-enhanced Raman scattering (SERS) exploits surface plasmons induced by the incident field in metallic nanostructures to significantly increase the Raman intensity. Graphene provides the ideal prototype two-dimensional (2d) test material to investigate SERS. Its Raman spectrum is well-known, graphene samples are entirely reproducible, height controllable down to the atomic scale, and can be made virtually defect-free. We report SERS from graphene, by depositing arrays of Au particles of well-defined dimensions on a graphene/SiO_2 (300 nm)/Si system. We detect significant enhancements at 633 nm. To elucidate the physics of SERS, we develop a quantitative analytical and numerical theory. The 2d nature of graphene allows for a closed-form description of the Raman enhancement, in agreement with experiments. We show that this scales with the nanoparticle cross section, the fourth power of the Mie enhancement, and is inversely proportional to the tenth power of the separation between graphene and the center of the nanoparticle. One important consequence is that metallic nanodisks are an ideal embodiment for SERS in 2d.

KEYWORDS: graphene · raman spectroscopy · plasmonics

Graphene is at the center of a significant research effort.[1−6] Near-ballistic transport at room temperature and high mobility[5−11] make it interesting for nanoelectronics,[12−15] especially for high frequency applications.[16] Furthermore, its optical and mechanical properties are ideal for micro- and nanomechanical systems, thin-film transistors, transparent and conductive electrodes, and photonics.[17−25] Graphene is also a test-bed for some long-standing problems, such as the Raman spectra of carbons.[26] Here we show that this conceptually simple material (due to its low-dimensionality) helps in understanding the basics of surface-enhanced Raman scattering (SERS).

Graphene layers can be identified by inelastic[26] and elastic light scattering.[27,28] Raman spectroscopy allows monitoring of doping, defects, strain, disorder, chemical modifications, and edges.[26,29−42] The Raman signal can be enhanced using certain substrates, such as the common Si+ SiO_2, due to interference in the SiO_2 layer, resulting into enhanced field amplitudes within graphene.[43−46]

Another way to increase the Raman signal is to perform SERS experiments.[47,48] SERS is widely used,[49−51] and enhancements as large as 14 orders of magnitude can be achieved (enough for single-molecule detection[52]). However, even though the technique is more than 30 years old,[51] the exact nature of SERS is still debated.[49] Furthermore, the particular mechanism might be different, depending on whether the Raman processes involved are resonant or not. In principle, even a single metallic nanostructure, *e.g.*, a metallic nanotip, can induce SERS at its apex, giving rise to the so-called tip-enhanced Raman scattering (TERS).[53−55] The key feature of TERS is its capability of optical sensing with high spatial resolution beyond the light diffraction limits.[56,57]

Most SERS-active systems studied to-date are based on random nanostructures, whose properties vary from experiment to experiment making quantitative comparison between theory and experiment difficult. Graphene offers a unique model system where SERS effects could be studied in detail. Its Raman spectrum is well-known,[26] being investigated in several hundreds of papers in the past 4 years. Graphene samples are very reproducible and offer an atomic-precision control on the number of layers, thus allowing a smooth transition from a purely 2d case to a 3d one. Furthermore, as both resonant and nonresonant Raman scattering can be in principle possible, such as in chemically modified graphene,[33] a distinction between different enhancement mechanisms could be made. Here we focus on the resonant case, where we believe the enhancement is mostly due to near-field plasmonic effects in the vicinity of metal particles.[47,53]

*Address correspondence to kostya@manchester.ac.uk; acf26@eng.cam.ac.uk.

Received for review May 17, 2010 and accepted August 31, 2010.

Published online September 21, 2010.
10.1021/nn1010842

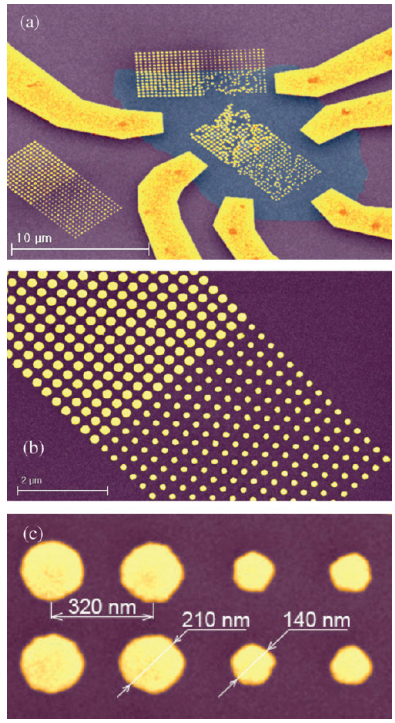

Figure 1. SEM images (in false colors) of our SERS sample: purple, SiO_2; bluish, graphene; yellow, Au electrodes and dots. (a) Overall image of the sample; (b,c) golden dots on SiO_2

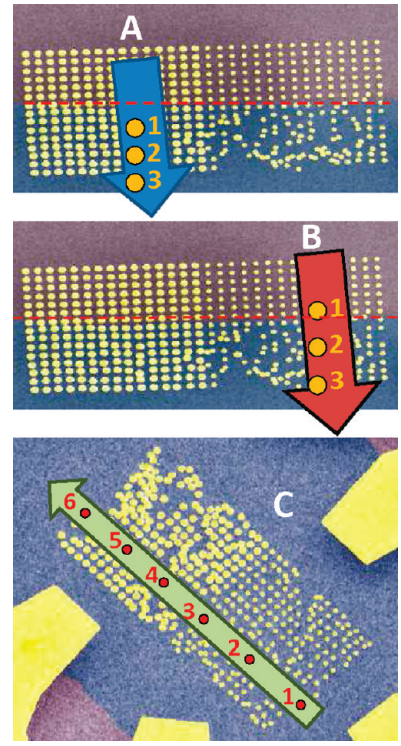

Figure 2. Raman linescans. Dotted red lines indicate the graphene edge. The intensity ratios are as follows. (A) Large dots: Point 1/Point 3; Point 2/Point 3. (B) Small dots: Point 1/Point 3; Point 2/Point 3. (C) Large dots: Point 4/Point 6; Point 5/Point 6; small dots: Point 3/Point 1; Point 2/Point 1

RESULTS AND DISCUSSION

Graphene flakes are prepared on Si+300 nm SiO_2 by micromechanical cleavage.[1] Single layer graphene (SLG) is identified by optical contrast[27,28] and Raman spectroscopy.[26] Electron beam lithography in combination with thin metallic film deposition (5 nm Cr+ 80 nm Au) and lift-off are utilized to prepare three sets of metallic dots, as well as a set of contacts for transport measurements, Figure 1. One set is placed directly on top of SLG, one partially covers it and partially rests on SiO_2, and the last is completely on SiO_2. The dot sizes and the configurations of the arrays can be seen on Figure 1. During lift-off, metallic dots are slightly shifted from their lithographically defined positions, probably by capillary forces. This indicates poor adhesion of Cr/Au dots onto graphene. Note that dots on SiO_2 still occupy the positions defined by the lithography procedure.

Raman spectra are recorded with a Renishaw RM1000 spectrometer, equipped with a piezoelectric stage (PI) able to shift the sample at nanometer steps. Line scans are recorded across the patterned arrays, as shown in Figures 2 and 3, for 488, 514, and 633 nm excitation.

The Raman enhancement is defined as the ratio of the Raman intensity measured on SLG covered by dots, compared to that measured outside the dots, but still on SLG, Figure 2. Figure 3 shows representative spectra measured at 633 nm. We consider both area, $A(2D)/A(G)$, and height, $I(2D)/I(G)$, ratios (see Methods). Figure 4 plots them for the two dot sizes and as a function of excitation energy. A clear enhancement is seen when comparing patterned and unpatterned SLG.

We model our experiments with the calculation box shown in Figure 5. Starting from the bottom, this consists of a semi-infinite Si substrate, 300 nm SiO_2, and a SLG of effective thickness 0.335 nm. On SLG, we have a Au/Cr disk with thickness 80 nm/5 nm, with the diameter set to either 140 or 210 nm, according to the experimental Au dot size. We time-integrate Maxwell's equations using the finite-difference time-domain method (FDTD)[58] as implemented in refs 59 and 60 (see Methods). For the absorbing boundary conditions in the vertical direction we use the perfectly matched-layer method (PML),[61] while in the lateral directions we use periodic boundary conditions simulating an infinite two-dimensional square array of Au/Cr nanodisks. We previously investigated the plasmonic resonances of similar nanoparticles (prepared in exactly the same conditions as in the present work).[62,63] This allowed us to extract the Au and Cr optical constants as obtained in our evaporators.[64] We also recently measured the optical constants of graphene by spectroscopic ellipsometry.[65] The dispersive materials Au, Cr, and graphene are described here by Drude−Lorentz models, each fitted to our experimental data. These are shown in Figure 11 in Methods. Finally, for simplicity we use $n = 1.46$ for SiO_2 and $n = 4$ for Si.[66]

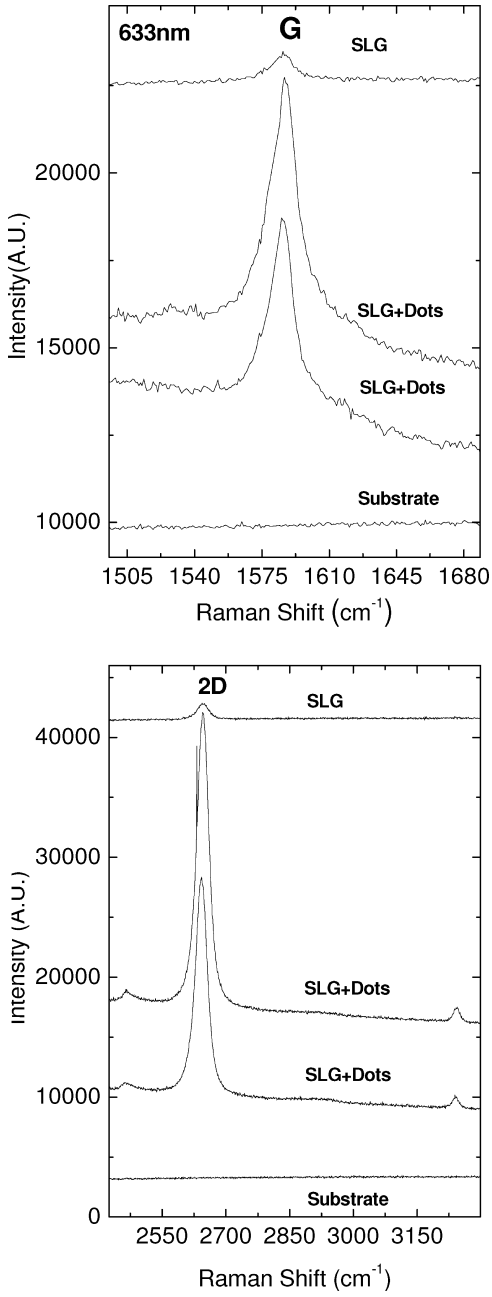

Figure 3. Representative Raman spectra measured across a line scan moving from outside to inside the Au dot patterned area for 633 excitation. An enhancement of all peaks is seen.

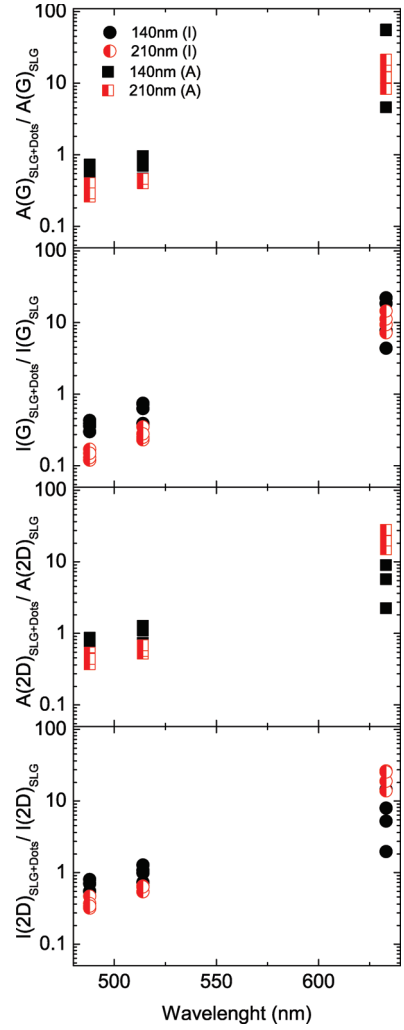

Figure 4. Ratio of height and areas of the G and 2D peaks measured on the patterned regions compared to those measured outside, as a function of the excitation energy, in a semilog scale.

We only consider normal incidence and emission, relevant for our Raman backscattering experiments. The incident field is a wide spectrum plane wave (*i.e.*, a narrow Gaussian temporal profile) coming from the top. We monitor the electric fields $E_x(r, t)$ and $E_y(r, t)$ at each grid point on the graphene plane, and upon Fourier transform we get the tangential-field amplitude $E_{||}(r, \omega)$ in frequency domain. This is enhanced compared to the incident field, due to substrate interference, and the surface plasmon resonance (SPR) near-field of the nanodisks.

We assume that the absorption at a particular point is proportional to the incident tangential field intensity. Furthermore, we assume that the Raman emission from a particular point is proportional to the corresponding Stokes-shifted incident intensity. Since the emitting dipole is not necessarily parallel to the driving field, we take the average of both parallel- and antiparallel-aligned dipoles. Finally, we assume the emission from points underneath the nanodisks to be reabsorbed and lost. We thus approximate the total Raman signal as[47]

$$I_{SERS} \propto \frac{1}{2}\int |E_{||}(\mathbf{r}, \omega)|^2 [|E_{||}(\mathbf{r}, \omega_s)|^2 + |E_{||}(\mathbf{r}', \omega_s)|^2]\, dS' \quad (1)$$

where $\mathbf{r}'$ indicates $\mathbf{r}$ rotated by $\pi/2$. The integration is performed over the area not directly underneath the nanodisks, and $\omega_s = \omega - \delta\omega$ is the Stokes shifted frequency. $\delta\omega = 2\pi c\nu$, where ν is the Raman shift (in cm^{-1}). The outcome of eq 1 is normalized by the corresponding calculation for suspended graphene (where the integral is over all the area since there are no nondisks to cover

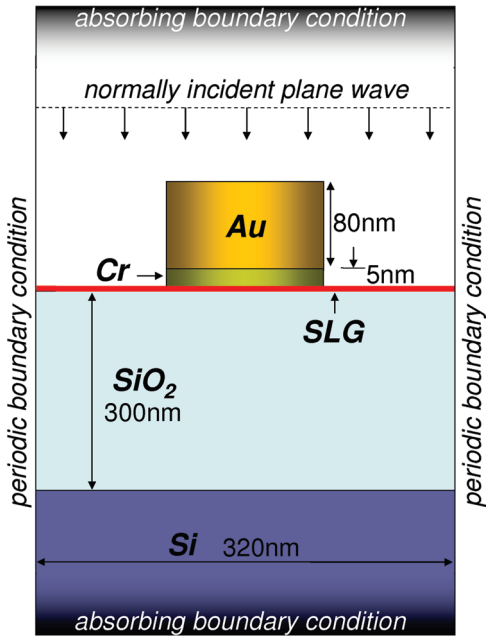

Figure 5. Simulation box: 80 nm/5 nm Au/Cr nanodisks on SLG/SiO_2/Si. The lateral periodicity is 320 nm. We consider diameters of 210 and 140 nm, corresponding to large and small dots.

the emission). We note that, given the large absorption of ~2.3% per graphene layer,[67] this approximation becomes questionable for local enhancements greater than ~43. We thus cut above 43. Emission saturation, on the other hand, cannot be reached because the Raman efficiency, even if larger than other materials due to the process being always resonant, is in absolute terms very small,[46] and would require ~10^{11} enhancement to exceed 100%.

The 300 nm SiO_2/Si substrate interferometrically increases not only the visibility[27,28] but also the Raman signal of graphene.[43,45,68] Here we expect an additional enhancement due to the Au nanodisks SPR near field. To distinguish between the two effects (substrate interference and SPR), we separately calculate both cases

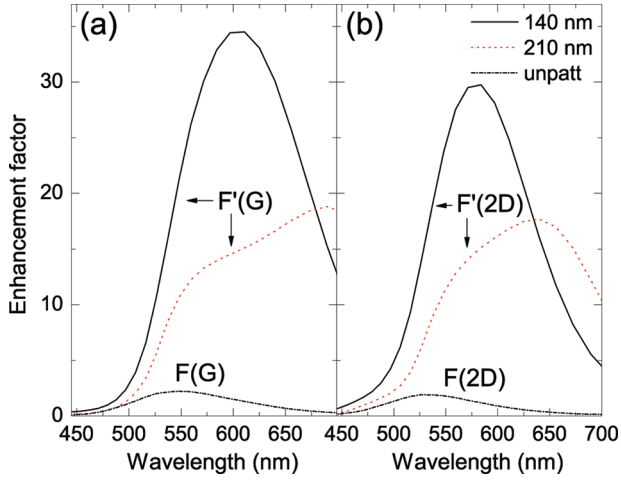

Figure 6. The total (patterned) enhancement factors for (a) the G and (b) 2D peaks. The dotted line is the corresponding interference (unpatterned) enhancement factor.

for unpatterned SLG on SiO_2/Si and SLG patterned with the Au nanodisks, still on SiO_2/Si. We define the interference enhancement factor F as the ratio of the Raman signal from unpatterned SLG on SiO_2/Si to that of suspended SLG, $F = I_{unpatt}/I_{susp}$, and the total enhancement factor F' as the ratio of the Raman signal from patterned SLG on SiO_2/Si to that of suspended SLG: $F' = I_{patt}/I_{susp} \equiv I_{SERS}/I_0$. Figure 6 plots such factors for the G and 2D peaks. This gives a maximum interference-related enhancement F at 550 nm of ~2.5 for the G peak and ~2 for the 2D. However, this is modest compared to the total enhancement F' when the nanodisks are taken into account. The total enhancement reaches up to 35, and is maximum at different wavelengths depending on the nanodisk diameter. The shoulder at 550 nm is likely related to interference, because (i) it is at the same frequency as the interference peak and (ii) it is stronger the further the plasmon peak.

There is a different enhancement for the two diameters, not only in peak value, but also in wavelength. This is mainly due to the increased size and fill factor of the 210 nm particles, both effects leading to a surface plasmon redshift.[69,70] Figure 7 plots the distribution of the tangential intensity enhancement in the SLG plane at 633 nm, which is approximately proportional to the absorption enhancement at that wavelength. Different patterns appear for the two sizes: the smaller disk exhibits a clear dipole pattern, while the larger disk pattern is modified. We then perform a simulation of the 210 nm disks for a 480 nm-period array, which is roughly the experimental fill factor of the 140 nm disk array. We find that, at the corresponding peak enhancement frequency, the intensity pattern acquires the characteristic dipole form seen in Figure 7a. Higher order multipoles may also give a small contribution to this difference, but not the dominant one, as can be verified by examining the Mie scattering coefficients[71,72] of the larger particles.

Figure 8 compares F'/F to the corresponding experimental Raman intensity ratios. Considering all approximations made, and the fact that some of the measurements were on top of distorted parts of the nanodisk arrays, the agreement is good. We find low enhancement for 488 and 514 nm, and large for 633 nm. Also, we reproduce a higher enhancement for the G peak in the small disks at 633 nm, and a similar enhancement for the 2D peak. The quantitative agreement for the 2D peak is not as good. However, this is expected given that its intensity significantly depends on electron−electron interactions, which could change in the presence of gold.[73]

The agreement between experiment and simulation is encouraging. It also allows us to get new physical insights into the SERS process of a 2d system, like graphene. The basic physics and detailed theory of the electromagnetic contribution to SERS on adsorbed molecules is well-known:[47] both absorption and emission

are enhanced due to interaction with surface plasmons, with an expected overall dependence on the fourth power of the SPR-mediated field enhancement.[47,74] However, a detailed theory for 2d systems is still lacking. Such formulation is challenging for our experiments: the Au particles do not have a regular spherical or ellipsoidal shape, they are large, so multipoles higher than dipole may contribute, there is a thin Cr layer, we are on SiO_2/Si giving additional interference and enhancement. We thus consider the simplified case of regular-shaped small Au particles inside a uniform medium. This provides all the new physics for SERS in graphene, or generally any 2d system. The final connection between experiments and theory will rely on simulations, covering different scales and experimental embodiments.

The generic system under study is depicted in Figure 9: at normal incidence, a plane wave of frequency ω excites a point dipole in the nanoparticle:

$$p \propto \alpha_{np}(\omega) \tag{2}$$

where the polarizability a_{np} is described by the Mie theory.[71,72] The poles of α_{np} define the optimal SERS frequencies. The reradiated near-field from this dipole scales as r^{-3}, and is responsible for the enhanced absorption. This will excite a Raman dipole:

$$p' \propto \alpha_R(\omega_s, \omega) r^{-3} \alpha_{np}(\omega) \tag{3}$$

where $\alpha_R(\omega_s, \omega)$ is the Raman polarizability and ω_s the Stokes-shifted emission frequency. This dipole near-field will in turn excite a secondary dipole in the nanoparticle:

$$p'' \propto \alpha_{np}(\omega_s) r^{-3} \alpha_R(\omega_s, \omega) r^{-3} \alpha_{np}(\omega) \tag{4}$$

now at the emission frequency ω_s. Thus, the additional surface-enhanced Raman signal is

$$\Delta I_{SERS} \propto \omega_s^4 \int |p''|^2 \, dS \tag{5}$$

where the integration is over the SLG area. For a square array with spacing L, normalizing to the corresponding Raman signal in the absence of the particles, the SERS enhancement is

$$\frac{\Delta I_{SERS}}{I_0} \approx \frac{3}{28} \sigma Q(\omega)^2 Q(\omega_s)^2 \left(\frac{a}{h}\right)^{10} \tag{6}$$

where a is the particle radius, h the separation between the particle center and the SLG plane, $\sigma = \pi a^2/L^2$ is its relative cross sectional area, and $Q(\omega) = |\alpha_{np}(\omega)|/(4\pi a^3)$ is the Mie enhancement. In general, Q depends on particle size and shape[72] (for spherical particles $\alpha_{np}(\omega)$ is given by eq 8 in Methods). In the limiting case of spherical particles with $a \ll \lambda$ the size dependence in the Mie enhancement is removed and $Q(\omega) \cong |[\varepsilon(\omega) - 1]/[\varepsilon(\omega) + 2]|$, where $\varepsilon(\omega)$ is the particle dielectric function.

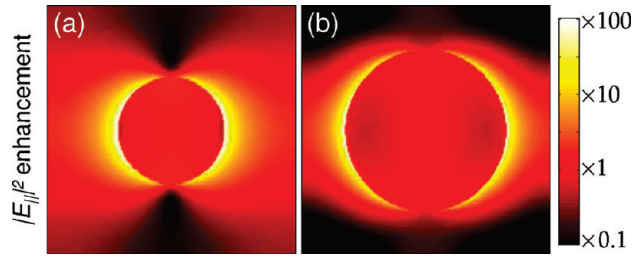

Figure 7. Tangential field intensity distribution at 633 nm for the (a) 140 nm and (b) 210 nm nanodisks.

This is our main theoretical result: the Raman enhancement scales with the metallic nanoparticle cross section, the fourth power of the Mie enhancement, and inversely with the tenth power of the separation between the nanoparticle center and graphene.

The above result is based on the assumption that SPR near-fields dominate the enhancement. However, for both large particles and separation distances, as in our experiments, this may become questionable. To have a useful comparison relevant to our experimental system, we derive in Methods (eq 24) the full expression for the SERS enhancement taking into account both radiative and nonradiative dipole fields.

Since eq 24 does not consider multiple reflections in the substrate, we compare it with FDTD simulations of Au nanospheres and nanodisks suspended in air, shown in Figure 10 for the G peak (where a small blueshift is due to the smaller effective refractive index below the suspended nanoparticles). In the absence of an analytical expression for the polarizability of a nanodisk, we use that of a sphere (see eq 8 in Methods). Also, to have a direct comparison, from the simulations we extract the pure SERS contribution ΔI_{SERS} by subtracting the incident from the total field.

We consider two sizes: 10 nm, to verify the small particle limit, and 140 nm, corresponding to the experiment. In both cases the aspect ratio corresponds to the experiment, *i.e.*, thickness/diameter = 80/140. The periodicity is also set to match the experiment with sur-

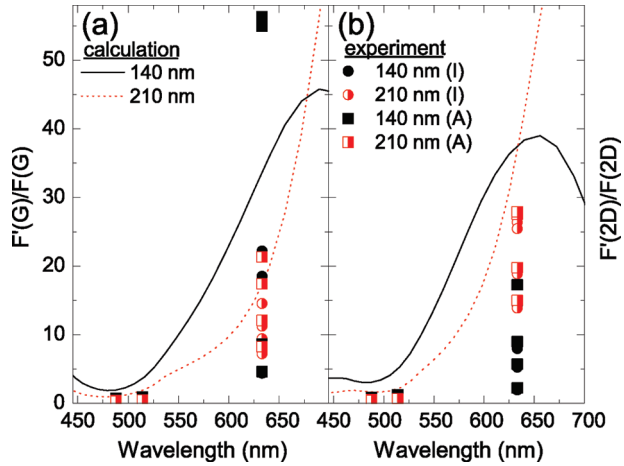

Figure 8. Normalized enhancement factors *F′*/*F* for (a) the G-band and (b) the 2D-band. Squares and circles are the experimental data.

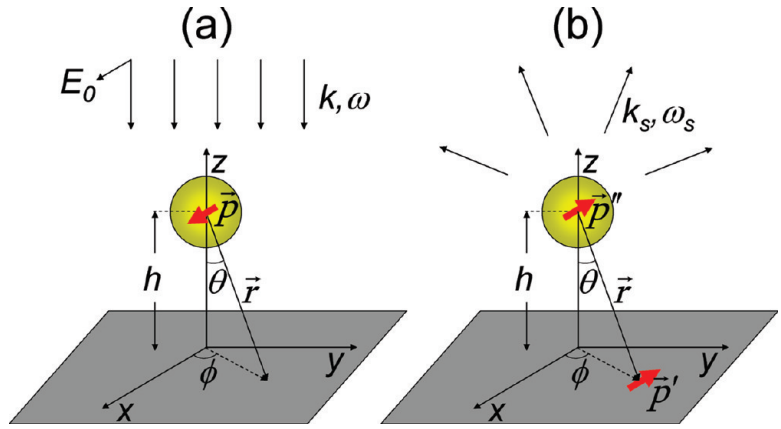

Figure 9. Scheme for SERS of a nanoparticle on graphene.

face filling ratio 15% (*i.e.*, 23 nm for 10 nm, and 320 nm for 140 nm). Figure 10 also plots the SERS predictions of eq 6 (near-field) and eq 24 (full-field). As expected, near-field and full-field coincide for the small particles, but differ for the large ones. The full-field calculation matches well the 140 nm sphere results, even for very large graphene−particle separations, confirming the validity of the dipole approximation at these particle sizes. The disks show a discrepancy at large distances, but a remarkably good agreement at small ones. The insets in Figure 10 plot the field distribution calculated by FDTD for the 10 nm Au sphere and the 140 nm Au disk, on a horizontal plane though the particle center. Both show characteristic dipole field patterns. This further confirms the validity of the dipole approximation for the larger particles, not only for spheres but also for disks. Overall, our analytical theory matches very well the simulations, capturing the essential physics of SERS in 2d.

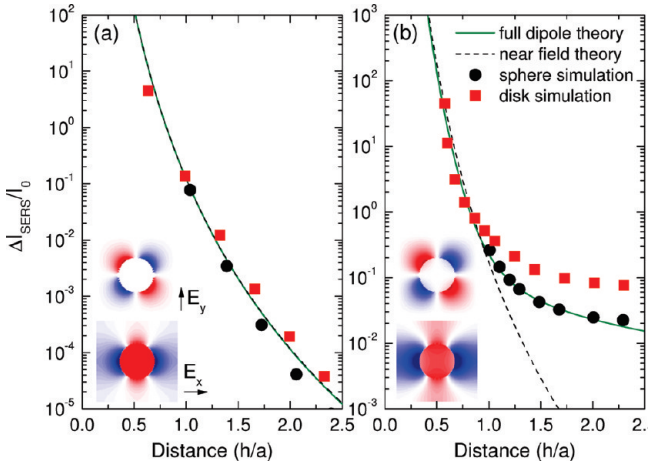

Figure 10. FDTD simulations of suspended nanospheres (circles) and nanodisks (squares) compared with the near-field theory of eq 6 (dashed line) and the full-field theory of eq 24 (solid line) for the G peak enhancement. The radius is (a) 10 nm and (b) 140 nm. For the disks the thickness/diameter ratio is 80/140, as for the experiment. Periodicities are 23 and 320 nm, with a 15% surface-filling ratio. The insets show the field distribution on a plane running through the nanoparticle center, at the corresponding maximum enhancement frequency (∼512 nm for 10 nm, and ∼520 nm for 140 nm). In (a) they are for the 10 nm sphere, in (b) they are for the 140 nm disk. Both show the characteristic dipole field distribution.

A very interesting consequence stems from Figure 10. For a sphere the minimum SLG-particle center distance cannot be less than the particle radius; *i.e.*, it must always be $h \geq a$. However, this is not true for disks. Thus, the expected enhancements are much higher for disks, with a good estimation given by eq 6 for $h < a$. Equation 6 thus becomes a valuable optimization/design tool. In particular, it identifies three steps to further improve SERS: (1) larger nanoparticle coverage σ, (2) larger Mie enhancement Q, (3) smaller nanoparticle-SLG separation h. The first is straightforward. The second is shape related, *e.g.*, ellipsoids have a different Q, which, for certain orientations, is stronger and redshifted compared to a sphere.[72] As for the third, flat oblate spheroids and thin disks have a smaller distance between their center and SLG. Thus, much larger enhancements are expected for flat spheroids and disks.

The analytical expressions derived in Methods can be extended to flakes of increasing number of layers, by vertical integration. Note, however, that if the number of layers is large, reflection becomes important (∼1% for 7 layers but >5% above 18 layers), and needs to be taken into account.

CONCLUSIONS

We studied SERS in graphene patterned with a square array of Au nanodisks on SiO_2 (300 nm)/Si. Significant enhancements were measured for both G and 2D bands at 633 nm. Similar results were obtained for both disk sizes. Large-scale FDTD simulations reproduce well the experiments. To elucidate the physics of SERS in 2d, we derived analytic expressions, and showed that taking into account the SPR near-fields only, a simple closed-form expression is found, where the Raman enhancement scales with the nanoparticle cross section, the fourth power of the Mie enhancement, and inversely with the tenth power of the separation between the nanoparticle center and graphene. This

points to thin nanodisks to achieve the highest SERS for 2d systems like graphene.

METHODS

Raman Background. The Raman spectrum of graphene consists of a set of distinct peaks. The G and D appear around 1580 and 1350 cm^{-1}, respectively. The G peak corresponds to the E_{2g} phonon at the Brillouin zone center. The D peak is due to the breathing modes of six-atom rings and requires a defect for its activation.[40,41,75,76] It comes from TO phonons around the **K** point,[40,41,76] is active by double resonance (DR),[75] and is strongly dispersive with excitation energy due to a Kohn anomaly at **K**.[31] DR can also happen as intravalley process, *i.e.*, connecting two points belonging to the same cone around **K** (or **K**′). This gives the so-called D′ peak, which is at ~1620 cm^{-1} in defected graphite measured at 514 nm. The 2D peak is the second order of the D peak. This is a single peak in SLG, whereas it splits in four in bilayer graphene BLG, reflecting the evolution of the band structure.[26] The 2D′ peak is the second order of D′. Since 2D and 2D′ originate from a process where momentum conservation is satisfied by two phonons with opposite wavevectors, no defects are required for their activation, and they are thus always present. Each Raman peak is characterized by position, width, height, and area. The frequency-integrated area under each peak represents the probability of the whole process. It is more robust with respect to various perturbations of the phonon states than width and height.[73] Indeed, for an ideal case of dispersionless undamped phonons with frequency ω_{ph}, the shape of the n-phonon peak is a Dirac δ distribution $\propto \delta(\omega - n\omega_{ph})$, with zero width, infinite height, but well-defined area. If the phonons decay (*e.g.*, into other phonons, due to anharmonicity, or into electron−hole pairs, due to electron−phonon coupling), the δ line shape broadens into a Lorentzian, but the area is preserved, as the total number of phonon states cannot be changed by such perturbations. If phonons have a weak dispersion, states with different momenta contribute at slightly different frequencies. This may result in an overall shift and a nontrivial peak shape, but frequency integration across the peak means counting all phonon states, as in the dispersionless case. Thus, the peak area is preserved, as long as the Raman matrix element itself is not changed significantly by the perturbation. The latter holds when the perturbation (phonon broadening or dispersion) is smaller than the typical energy scale determining the matrix element. Converting this into a time scale using the uncertainty principle we have that, if the Raman process is faster than the phonon decay, the total number of photons emitted within a given peak (*i.e.*, integrated over frequency across the peak), is not affected by phonon decay, although their spectral distribution can be. Even if the graphene phonons giving rise to the D and D′ peaks are dispersive,[31] their relative change with respect to the average phonon energy is at most a few %, thus we are in the weakly dispersive case. The phonon decay in graphene is in the ps time scale, while the Raman process is faster, in the fs time scale.[30,77,78] We thus consider both the area, $A(2D)/A(G)$, and height, $I(2D)/I(G)$, ratios.

SERS Calculations. Let us consider a generic configuration as in Figure 9, comprising a Au spherical particle of radius a at distance h from SLG, normal plane wave incidence, with field amplitude E_0, frequency ω, and polarization along x. The reradiated fields are due to an induced electric dipole at its center:

$$\mathbf{p} = \varepsilon_0 \alpha_{np}(\omega)\mathbf{E} \approx \varepsilon_0 \alpha_{np}(\omega) E_0 \hat{\mathbf{x}} \tag{7}$$

where E is the local field at the nanoparticle, modified from the incident one due to the presence of SLG. The SLG normal incidence reflectance is almost zero[67] and, due to continuity, the local field can be taken approximately the same as the incident one. This is further corroborated from calculations of the depolarization matrix of single wall nanotubes, where for polarization along the axis, no depolarization is found.[53,79] The polarizability a_{np} for a sphere in the Mie theory[71,72] is

$$\alpha_{np}(\omega) = \frac{6\pi i}{k^3} \cdot \frac{\tilde{n}\psi_1(\tilde{n}ka)\psi_1'(ka) - \psi_1(ka)\psi_1'(\tilde{n}ka)}{\tilde{n}\psi_1(\tilde{n}ka)\xi_1'(ka) - \xi_1(ka)\psi_1'(\tilde{n}ka)} \tag{8}$$

where ψ_1 and ξ_1 are the Riccati−Bessel functions, $k = \omega/c$ and $\tilde{n} \equiv \tilde{n}(\omega)$ is the nanoparticle complex index of refraction. In general, the refractive index of metallic nanoparticles differs from the bulk value due the reduced free electron relaxation caused by electron surface scattering.[59,80] However, we have relatively large particles, where this correction is negligible. Thus we use the bulk Au refractive index. If the nanoparticle is much smaller than the wavelength, eq 8 simplifies:[72]

$$\alpha_{np}(\omega) \approx 4\pi a^3 \frac{\varepsilon(\omega) - 1}{\varepsilon(\omega) + 2} \tag{9}$$

with $\varepsilon(\omega) = \tilde{n}^2(\omega)$ the nanoparticle dielectric function.

The total field at position $\mathbf{r}$ on SLG is[81]

$$\mathbf{E}_t(\mathbf{r},\omega) \approx E_0(\mathbf{r},\omega)\hat{\mathbf{x}} + \frac{e^{ikr}}{4\pi\varepsilon_0}\left[\frac{k^2}{r}\hat{\mathbf{r}} \times (\mathbf{p} \times \hat{\mathbf{r}}) + \left(\frac{1}{r^3} - \frac{ik}{r^2}\right)[3\hat{\mathbf{r}}(\hat{\mathbf{r}}\cdot\mathbf{p}) - \mathbf{p}]\right] \tag{10}$$

The first term in the square bracket is the radiation-field, while the second is the near-field. They scale with distance and wavelength as $(\lambda^2 r)^{-1}$ and r^{-3}, $(\lambda r^2)^{-1}$, respectively. Assuming the nanoparticle distance from SLG to be much smaller than the wavelength, $r \ll \lambda$, and the resonant near-field much larger than the incident field E_0, then the near-field r^{-3} dominates. Its transverse component drives the SLG enhanced absorption. Simultaneously, the Raman emitted field also interacts with the Au particle SPR, further enhancing the total Raman emission. To fully explore both processes, we need: (1) total absorption enhancement; (2) total Raman enhancement.

Absorption Enhancement. The additional absorption in graphene is due to the enhanced near-field. Absorption is defined as current × field,[81] thus approximated as

$$\Delta A = G_0 \int |\mathbf{E}_{t_{||}}^{nf}|^2 \, dS \tag{11}$$

where $G_0 = e^2/(4\hbar)$ is graphene's dynamical (optical) sheet conductance.[67,82−85] Combining, the near-field transverse component of the driving field is

$$|\mathbf{E}_{t_{||}}^{nf}(\omega)| = E_0 Q(\omega) a^3 r^{-3} |[3\hat{\mathbf{r}}(\hat{\mathbf{r}}\cdot\hat{\mathbf{x}}) - \hat{\mathbf{x}}]_{||}| \tag{12}$$

with $Q(\omega) = |\alpha_{np}(\omega)|/(4\pi a^3)$. In the above we ignore cross terms between incident and reradiated fields. This is justified when strong near-field enhancements are expected (as should be for SERS), but less so when the near-fields are of the same order as the incident field.

From Figure 9, $x = r\sin\theta\cos\phi$, $y = r\sin\theta\sin\phi$, and $z = r\cos\theta$, while $r = h/\cos\theta$. The integration surface element is $\rho\, d\rho\, d\phi = h^2 \sin\theta \cos^{-3}\theta\, d\phi\, d\theta$, where $\rho = h\tan\theta$ is $\mathbf{r}$'s projection on the plane. Equation 11 then becomes

$$\Delta A = \frac{G_0 E_0^2 Q^2 a^6}{h^4} \int_0^{\pi/2} \int_0^{2\pi} \cos^3\theta \sin\theta\, f(\theta,\phi)\, d\phi\, d\theta \tag{13}$$

with $f(\theta,\phi) = 9\sin^4\theta\cos^2\phi - 6\sin^2\theta\cos^2\phi + 1$. Then

$$\Delta A = \frac{3\pi G_0 E_0^2 Q^2(\omega) a^6}{8h^4} \tag{14}$$

For a square lattice with spacing L, the absorption enhancement becomes:

$$\frac{\Delta A}{A_0} = \frac{3\pi Q^2(\omega) a^6}{8h^4 L^2} = \frac{3}{8}\sigma Q^2(\omega)\left(\frac{a}{h}\right)^4 \tag{15}$$

where $\sigma = \pi a^2/L^2$ is the nanoparticle relative cross section. For spheres directly placed on SLG, *i.e.*, $h = a$, eq 15 simplifies to

$$\frac{\Delta A}{A_0} = \frac{3}{8}\sigma Q^2(\omega) \tag{16}$$

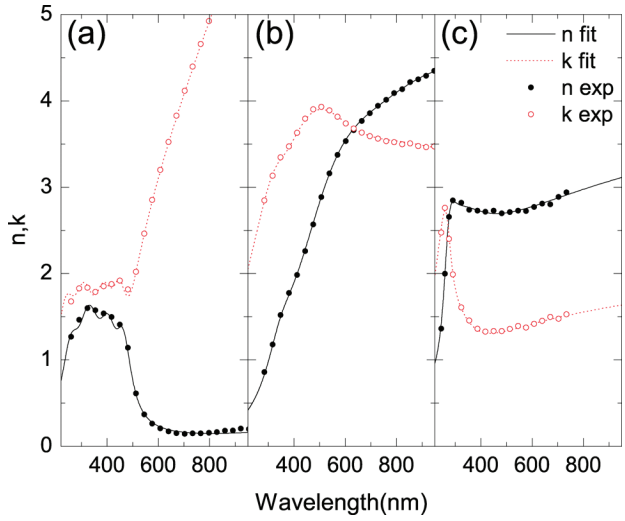

Figure 11. The refractive indices used in the calculations for (a) Au, (b) Cr, and (c) SLG. Open and solid circles indicate the corresponding experimental data.[64,65]

We remind here that in the $a \ll \lambda$ limit, the Mie enhancement is $Q(\omega) = |[\varepsilon(\omega) - 1]/[\varepsilon(\omega) + 2]|$.

Raman Enhancement. Going back to eq 12, $\mathbf{E}^{nf}_{t_\parallel}(\omega)$ will excite a dipole field on SLG at the Raman frequency ω_s:

$$\mathbf{p}' = \alpha_R(\omega_s, \omega)|\mathbf{E}^{nf}_{t_\parallel}|\hat{\mathbf{p}}' \tag{17}$$

The polarization of the Raman dipole is not necessarily the same as that of the driving field. Thus, for generality we assume this to be randomly polarized on the SLG plane. In this case it suffices to take the average of two dipoles, one polarized along $\hat{\mathbf{x}}$, and another along $\hat{\mathbf{y}}$. The one along $\hat{\mathbf{x}}$ will emit as the dipole term of eq 10. We are again interested in the dominant near-field term that decays as r^{-3}. This will get coupled to the nanoparticle and thus SPR enhanced. It will excite a secondary dipole at the nanoparticle:

$$p'' = Q(\omega_s)\,\alpha_R(\omega_s, \omega)\,Q(\omega)E_0a^6r^{-6}|[3\hat{\mathbf{r}}(\hat{\mathbf{r}}\cdot\hat{\mathbf{x}}) - \hat{\mathbf{x}}]_\parallel|^2 \tag{18}$$

where we again consider the projection of the dipole given the backscattering geometry considered here. The radiated flux can be taken as the additional surface-enhanced Raman signal:

$$\Delta I_{SERS} = \frac{ck_s^4}{24\pi\varepsilon_0}\int p''^2\,dS \tag{19}$$

where $k_s = \omega_s/c$ and we multiply by a factor $^1/_2$ since we only consider the upper half flux. Using the angular relationships for x, y, z and dS we get:

$$\Delta I_{SERS} = \frac{ck_s^4E_0^2Q^2(\omega)\,Q^2(\omega_s)\,a^{12}}{24\pi\varepsilon_0h^{10}}|\alpha_R(\omega_s, \omega)|^2 \times \int_0^{\pi/2}\int_0^{2\pi}\cos^9\theta\,\sin\theta\,f_x(\theta,\phi)\,d\phi\,d\theta \tag{20}$$

where $f_x(\theta, \phi) = 81\sin^8\theta\cos^4\phi - 108\sin^6\theta\cos^4\phi + 18\sin^4\theta\cos^2\phi(1 + 2\cos^2\phi) - 12\sin^2\theta\cos^2\phi + 1$. The angular integration yields $33\pi/280$. For the calculation with the Raman dipole along $\mathbf{y}$, the angular part of eq 18 becomes $|[3\hat{\mathbf{r}}(\hat{\mathbf{r}}\cdot\hat{\mathbf{x}}) - \hat{\mathbf{x}}]_\parallel|[3\hat{\mathbf{r}}(\hat{\mathbf{r}}\cdot\hat{\mathbf{y}}) - \hat{\mathbf{y}}]_\parallel|$ with a slightly different $f_y(\theta, \phi)$, but a similar angular integration value of $27\pi/280$. The average angular contribution is $3\pi/28$. Thus the additional Raman signal can be written as

$$\Delta I_{SERS} \approx \frac{3\pi}{28}\frac{ck_s^4E_0^2Q^2(\omega)Q^2(\omega_s)a^{12}}{24\pi\varepsilon_0h^{10}}|\alpha_R(\omega_s, \omega)|^2 \tag{21}$$

To evaluate the enhancement factor, we normalize to the expected signal I_0 in the absence of nanoparticles. Considering a square unit cell of side equal to the nanoparticle spacing L, we get

$$I_0 \approx L^2\frac{ck_s^4E_0^2}{24\pi\varepsilon_0}|\alpha_R(\omega_s, \omega)|^2 \tag{22}$$

The Raman enhancement factor is

$$\frac{\Delta I_{SERS}}{I_0} \approx \frac{3}{28}\sigma Q^2(\omega)Q^2(\omega_s)\left(\frac{a}{h}\right)^{10} \tag{23}$$

In the above we took into account only the $\sim r^{-3}$ near-field dipole term. For SERS this is indeed the dominant contribution. However, for a detailed comparison between theory and simulation for large particles and large particle−graphene separations, this may not be enough. In particular, the $(\lambda^2 r)^{-1}$ and $(\lambda r^2)^{-1}$ terms of eq 10 may become important. To facilitate such a comparison and explicitly test the dipole model, we perform the Raman integration taking all dipole fields into account (we again ignore cross terms with the incident radiation though). This gives

$$\frac{\Delta I_{SERS}}{I_0} = \sigma Q^2(\omega)\,Q^2(\omega_s)\,F(a, k, k_s, h) \tag{24}$$

where

$$F(a, k, k_s, h) = \frac{3}{28}\left(\frac{a}{h}\right)^{10} - \frac{141}{2240}a^2(k^2 + k_s^2)\left(\frac{a}{h}\right)^8 + \frac{72}{420}a^4(k^2k_s^2)\left(\frac{a}{h}\right)^6 + \frac{79}{420}a^4(k^4 + k_s^4)\left(\frac{a}{h}\right)^6 - \frac{23}{120}a^6(k^4k_s^2 + k^2k_s^4)\left(\frac{a}{h}\right)^4 + \frac{7}{15}a^8(k^4k_s^4)\left(\frac{a}{h}\right)^2 \tag{25}$$

Equation 25 includes the average of both polarizations, similarly to what was done for eq 21.

Finite-Difference Time-Domain Method. In the FDTD method, Maxwell's equations are time-integrated on a computational grid:

$$\nabla\times\mathbf{E} = -\mu\partial_t\mathbf{H} \tag{26}$$

$$\nabla\times\mathbf{H} = \varepsilon_0\varepsilon_\infty\partial_t\mathbf{E} + \partial_t\mathbf{P}_0 + \sum_{j=1}^{N}\partial_t\mathbf{P}_j \tag{27}$$

where material polarization is taken into account through polarizabilities $\mathbf{P}$:

$$\partial_t^2\mathbf{P}_0 + \gamma\partial_t\mathbf{P}_0 = \omega_p^2\varepsilon_0\mathbf{E} \tag{28}$$

$$\partial_t^2\mathbf{P}_j + \Gamma_j\partial_t\mathbf{P}_j + \Omega_j^2\mathbf{P}_j = \Delta\varepsilon_j\Omega_j^2\varepsilon_0\mathbf{E} \tag{29}$$

This gives a Drude−Lorentz model for the dielectric function:[86]

$$\varepsilon(\omega) = \varepsilon_\infty - \frac{\omega_p^2}{\omega^2 + i\omega\gamma} + \sum_{j=1}^{N}\frac{\Delta\varepsilon_j\Omega_j^2}{\Omega_j^2 - \omega^2 - i\omega\Gamma_j} \tag{30}$$

where the first term is the Drude free-electron contribution and the second contains Lorentz oscillators corresponding to interband transitions. ω_p and $1/\gamma$ are the free electron plasma frequency and relaxation time, Ω_j, $\Delta\varepsilon_j$, and Γ_j are transition frequency, oscillator strength, and decay rate for the Lorentz terms. To accurately reproduce the experimental dielectric functions (Au and Cr from ref 64; SLG from ref 65) we treat these as fit parameters. For Au we use $N = 4$, and $\varepsilon_\infty = 3.454$, $\Delta\varepsilon_j = (0.376, 0.63, 1.208, 1.124)$, $\hbar\omega_p = 8.73$ eV, $\hbar\gamma = 0.046$ eV, $\hbar\Omega_j = (2.72, 3.13, 3.88, 4.95)$ eV, and $\hbar\Gamma_j = (0.39, 0.655, 1.16, 1.67)$ eV. For Cr we use $N = 3$, and $\varepsilon_\infty = 1$, $\Delta\varepsilon_j = (9.54, 15.5, 1.1)$, $\hbar\omega_p = 5.51$ eV, $\hbar\gamma = 0.731$ eV, $\hbar\Omega_j = (1.43, 2.36, 3.64)$ eV, and $\hbar\Gamma_j = (1.19, 1.94, 1.41)$ eV. Finally, for SLG we use $N = 3$, and $\varepsilon_\infty = 1.964$, $\Delta\varepsilon_j = (6.99, 1.69, 1.53)$, $\hbar\omega_p = 6.02$ eV, $\hbar\gamma = 4.52$ eV, $\hbar\Omega_j = (3.14, 4.03,$

4.59) eV, and $\hbar\Gamma_j$ = (7.99, 2.01, 0.88) eV. Figure 11 plots our model dielectric functions along with the experimental ones, showing an excellent agreement.

To account for the SLG thickness and still keep the simulation reasonably fast, we employ an anisotropic grid with 0.335 nm spacing in the vertical dimension and 2 nm in the lateral one. By calculations on smaller cells we verified that such a grid introduces small errors, typically less than 5% and never exceeding 10%. Considering our approximations up to this point (normal incidence and those in eq 1, we find this to be well within the overall simulation errors.

Acknowledgment. ACF acknowledges funding from the Royal Society, the ERC Grant NANOPOTS, and EPSRC Grant EP/G042357/1. The authors acknowledge computing time at the Research Center for Scientific Simulations (RCSS) at the University of Ioannina.

REFERENCES AND NOTES

1. Novoselov, K. S.; Geim, A. K.; Morozov, S. V.; Jiang, D.; Zhang, Y.; Dubonos, S. V.; Grigorieva, I. V.; Firsov, A. A. Electric Field Effect in Atomically Thin Carbon Films. *Science* **2004**, *306*, 666–669.
2. Geim, A. K.; Novoselov, K. S. The Rise of Graphene. *Nat. Mater.* **2007**, *6*, 183–191.
3. Castro Neto, A. H.; Guinea, F.; Peres, N. M. R.; Novoselov, K. S.; Geim, A. K. The Electronic Properties Of Graphene. *Rev. Mod. Phys.* **2009**, *81*, 109–162.
4. Charlier, J. C.; Eklund, P. C.; Zhu, J.; Ferrari, A. C. Electron and Phonon Properties of Graphene: Their Relationship with Carbon Nanotubes. *Topics Appl. Phys.* **2008**, *111*, 673–709.
5. Novoselov, K. S.; Geim, A. K.; Morozov, S. V.; Jiang, D.; Katsnelson, M. I.; Grigorieva, I. V.; Dubonos, S. V.; Firsov, A. A. Two-Dimensional Gas of Massless Dirac Fermions in Graphene. *Nature (London)* **2005**, *438*, 197–200.
6. Zhang, Y.; Tan, Y. W.; Stormer, H. L.; Kim, P. Experimental Observation of the Quantum Hall Effect and Berry's Phase in Graphene. *Nature (London)* **2005**, *438*, 201–204.
7. Novoselov, K. S.; Jiang, Z.; Zhang, Y.; Morozov, S. V.; Stormer, H. L.; Zeitler, U.; Maan, J. C.; Boebinger, G. S.; Kim, P.; Geim, A. K. Room-Temperature Quantum Hall Effect in Graphene. *Science* **2007**, *315*, 1379.
8. Morozov, S. V.; Novoselov, K. S.; Katsnelson, M. I.; Schedin, F.; Elias, D. C.; Jaszczak, J. A.; Geim, A. K. Giant Intrinsic Carrier Mobilities in Graphene and Its Bilayer. *Phys. Rev. Lett.* **2008**, *100*, 016602.
9. Du, X.; Skachko, I.; Barker, A.; Andrei, E. Y. Approaching Ballistic Transport in Suspended Graphene. *Nat. Nanotechnol.* **2008**, *3*, 491–495.
10. Bolotin, K. I.; Sikes, K. J.; Hone, J.; Stormer, H. L.; Kim., P. Temperature-Dependent Transport in Suspended Graphene. *Phys. Rev. Lett.* **2008**, *101*, 096802.
11. Bolotin, K. I.; Sikes, K. J.; Jiang, Z.; Fundenberg, G.; Hone, J.; Kim, P.; Stormer, H. L. Ultrahigh Electron Mobility in Suspended Graphene. *Solid State Commun.* **2008**, *146*, 351–355.
12. Han, M. Y.; Oezylmaz, B.; Zhang, Y.; Kim, P. Energy Band-Gap Engineering of Graphene Nanoribbons. *Phys. Rev. Lett.* **2007**, *98*, 206805.
13. Chen, Z.; Lin, Y. M.; Rooks, M.; Avouris, P. Graphene Nano-Ribbon Electronics. *Phys. E* **2007**, *40*, 228–232.
14. Zhang, Y.; Small, J. P.; Pontius, W. V.; Kim, P. Fabrication and Electric-Field-Dependent Transport Measurements of Mesoscopic Graphite Devices. *Appl. Phys. Lett.* **2005**, *86*, 073104.
15. Lemme, M. C.; Echtermeyer, T. J.; Baus, M.; Kurz, H. A Graphene Field-Effect Device. *IEEE Electron. Dev. Lett.* **2007**, *28*, 282–284.
16. Lin, Y. M.; Jenkins, K. A.; Valdes-Garcia, A.; Small, J. P.; Farmer, D. B.; Avouris, P. Operation of Graphene Transistors at Gigahertz Frequencies. *Nano Lett.* **2009**, *9*, 422–426.
17. Bunch, J. S.; van der Zande, A. M.; Verbridge, S. S.; Frank, I. W.; Tanenbaum, D. M.; Parpia, J. M.; Craighead, H. G.; McEuen, P. L. Electromechanical Resonators from Graphene Sheets. *Science* **2007**, *315*, 490–493.
18. Blake, P.; Brimicombe, P. D.; Nair, R. R.; Booth, T. J.; Jiang, D.; Schedin, F.; Ponomarenko, L. A.; Morozov, S. V.; Gleeson, H. F.; Hill, E. W. Graphene-Based Liquid Crystal Device. *Nano Lett.* **2008**, *8*, 1704–1708.
19. Hernandez, Y.; Nicolosi, V.; Lotya, M.; Blighe, F.; Sun, Z.; De, S.; McGovern, I. T.; Holland, B.; Byrne, M.; Gunko, Y. High-Yield Production of Graphene by Liquid-Phase Exfoliation of Graphite. *Nat. Nanotechnol.* **2008**, *3*, 563–568.
20. Eda, G.; Fanchini, G.; Chhowalla, M. Large-Area Ultrathin Films of Reduced Graphene Oxide as a Transparent and Flexible Electronic Material. *Nat. Nanotechnol.* **2008**, *3*, 270–274.
21. Sun, Z.; Hasan, T.; Torrisi, F.; Popa, D.; Privitera, G.; Wang, F.; Bonaccorso, F.; Basko, D. M.; Ferrari, A. C. Graphene Mode-Locked Ultrafast Laser. *ACS Nano* **2010**, *4*, 803–810.
22. Hasan, T.; Sun, Z.; Wang, F.; Bonaccorso, F.; Tan, P. H.; Rozhin, A. G.; Ferrari, A. C. Nanotube-Polymer Composites for Ultrafast Photonics. *Adv. Mater.* **2009**, *21*, 3874–3899.
23. Gokus, T.; Nair, R. R.; Bonetti, A.; Bhmler, M.; Lombardo, A.; Novoselov, K. S.; Geim, A. K.; Ferrari, A. C.; Hartschuh, A. Making Graphene Luminescent by Oxygen Plasma Treatment. *ACS Nano* **2009**, *3*, 3963–3968.
24. Essig, S.; Marquardt, C. W.; Vijayaraghavan, A.; Ganzhorn, M.; Dehm, S.; Hennrich, F.; Ou, F.; Green, A. A.; Sciascia, C.; Bonaccorso, F. Phonon-Assisted Electroluminescence from Metallic Carbon Nanotubes and Graphene. *Nano Lett.* **2010**, *10*, 1589–1594.
25. Bonaccorso, F.; Sun, Z.; Hasan, T.; Ferrari, A. C. Graphene Photonics and Optoelectronics. *Nature Photonics* **2010**, *4*, 611–622.
26. Ferrari, A. C.; Meyer, J. C.; Scardaci, V.; Casiraghi, C.; Lazzeri, M.; Mauri, F.; Piscanec, S.; Jiang, D.; Novoselov, K. S.; Roth, S.; Geim, A. K. Raman Spectrum of Graphene and Graphene Layers. *Phys. Rev. Lett.* **2006**, *97*, 187401.
27. Casiraghi, C.; Hartschuh, A.; Lidorikis, E.; Qian, H.; Harutyunyan, H.; Gokus, T.; Novoselov, K. S.; Ferrari, A. C. Rayleigh Imaging of Graphene and Graphene Layers. *Nano Lett.* **2007**, *7*, 2711–2717.
28. Blake, P.; Hill, E. W.; Castro Neto, A. H.; Novoselov, K. S.; Jiang, D.; Yang, R.; Booth, T. J.; Geim, A. K. Making Graphene Visible. *Appl. Phys. Lett.* **2007**, *91*, 063124.
29. Casiraghi, C.; Pisana, S.; Novoselov, K. S.; Geim, A. K.; Ferrari, A. C. Raman Fingerprint of Charged Impurities in Graphene. *Appl. Phys. Lett.* **2007**, *91*, 233108.
30. Pisana, S.; Lazzeri, M.; Casiraghi, C.; Novoselov, K. S.; Geim, A. K.; Ferrari, A. C.; Mauri, F. Breakdown of the Adiabatic Born Oppenheimer Approximation in Graphene. *Nat. Mater.* **2007**, *6*, 198–201.
31. Piscanec, S.; Lazzeri, M.; Mauri, F.; Ferrari, A. C.; Robertson, J. Kohn Anomalies and Electron-Phonon Interactions in Graphite. *Phys. Rev. Lett.* **2004**, *93*, 185503.
32. Casiraghi, C.; Hartschuh, A.; Qian, H.; Piscanec, S.; Georgi, C.; Fasoli, A.; Novoselov, K. S.; Basko, D. M.; Ferrari, A. C. Raman Spectroscopy of Graphene Edges. *Nano Lett.* **2009**, *9*, 1433–1441.
33. Elias, D. C.; Nair, R. R.; Mohiuddin, T. M. G.; Morozov, S. V.; Blake, P.; Halsall, M. P.; Ferrari, A. C.; Boukhvalov, D. W.; Katsnelson, M. I.; Geim, A. K.; Novoselov, K. S. Control of Graphene's Properties by Reversible Hydrogenation: Evidence for Graphane. *Science* **2009**, *323*, 610–613.
34. Ferrari, A. C. Raman Spectroscopy of Graphene and Graphite: Disorder, Electron Phonon Coupling, Doping and Nonadiabatic Effects. *Solid State Commun.* **2007**, *143*, 47–57.
35. Das, A.; Pisana, S.; Piscanec, S.; Chakraborty, B.; Saha, S. K.; Waghmare, U. V.; Yang, R.; Krishnamurhthy, H. R.; Geim, A. K.; Ferrari, A. C.; Sood, A. K. Monitoring Dopants by Raman Scattering in an Electrochemically Top-Gated Graphene Transistor. *Nature Nanotechnol.* **2008**, *3*, 210–215.
36. Das, A.; Chakraborty, B.; Piscanec, S.; Pisana, S.; Sood, A. K.; Ferrari, A. C. Phonon Renormalization In Doped Bilayer Graphene. *Phys. Rev. B* **2009**, *79*, 155417.

37. Mohiuddin, T. M. G.; Lombardo, A.; Nair, R. R.; Bonetti, A.; Savini, G.; Jalil, R.; Bonini, N.; Basko, D. M.; Galiotis, C.; Marzari, N. Uniaxial Strain in Graphene by Raman Spectroscopy: G Peak Splitting, Gruneisen Parameters, and Sample Orientation. *Phys. Rev. B* **2009**, *79*, 205433.
38. Yan, J.; Zhang, Y.; Kim, P.; Pinczuk, A. Electric Field Effect Tuning of Electron-Phonon Coupling in Graphene. *Phys. Rev. Lett.* **2007**, *98*, 166802.
39. Graf, D.; Molitor, F.; Ensslin, K.; Stampfer, C.; Jungen, A.; Hierold, C.; Wirtz, L. Spatially Resolved Raman Spectroscopy of Single- And Few-Layer Graphene. *Nano Lett.* **2007**, *7*, 238–242.
40. Ferrari, A. C.; Robertson, J. Interpretation of Raman Spectra of Disordered and Amorphous Carbon. *Phys. Rev. B* **2000**, *61*, 14095–14107.
41. Ferrari, A. C.; Robertson, J. Resonant Raman Spectroscopy of Disordered, Amorphous, And Diamondlike Carbon. *Phys. Rev. B* **2001**, *64*, 075414.
42. Ferrari, A. C.; Robertson, J. Raman Spectroscopy In Carbons: From Nanotubes To Diamond. *Philos. Trans. R. Soc., A* **2004**, *362*, 2269–2565.
43. Wang, Y. Y.; Ni, Z. H.; Shen, Z. X.; Wang, H. M.; Wu, Y. H. Interference Enhancement of Raman Signal of Graphene. *Appl. Phys. Lett.* **2008**, *92*, 043121.
44. Yoon, D.; Moon, H.; Son, Y.-W.; Choi, J. S.; Park, B. H.; Cha, Y. H.; Kim, Y. D.; Cheong, H. Interference Effect on Raman Spectrum of Graphene on SiO_2/Si. *Phys. Rev. B* **2009**, *80*, 125422.
45. Gao, L.; Ren, W.; Liu, B.; Saito, R.; Wu, Z.-S.; Li, S.; Jiang, C.; Li, F.; Cheng, H.-M. Surface and Interference Coenhanced Raman Scattering of Graphene. *ACS Nano* **2009**, *3*, 933–939.
46. Klar, P.; Lidorikis, E.; Eckmann, A.; Panknin, R.; Ferrari, A. C.; Casiraghi, C. Raman Scattering Efficiency of Graphene. Submitted for publication, 2010.
47. Moskovits, M. Surface-Enhanced Spectroscopy. *Rev. Mod. Phys.* **1985**, *57*, 783–826.
48. Kneipp, K.; Moskovits, M.; Kneipp, K., Eds. *Surface-Enhanced Raman Scattering: Physics and Applications*; Springer-Verlag: Berlin, Heidelberg, 2006.
49. Jensen, L.; Aikens, C. M.; Schatz, G. C. Electronic Structure Methods for Studying Surface-Enhanced Raman Scattering. *Chem. Soc. Rev.* **2008**, *37*, 1061–1073.
50. Kneipp, K.; Kneipp, H.; Itzkan, I.; Dasari, R. R.; Feld, M. S. Surface-Enhanced Raman Scattering and Biophysics. *J. Phys.: Condens. Matter* **2002**, *14*, R597–R624.
51. Fleischmann, M.; Hendra, P. J.; McQuillan, A. J. Raman Spectra of Pyridine Adsorbed at a Silver Electrode. *Chem. Phys. Lett.* **1974**, *26*, 163–166.
52. Nie, S.; Emory, S. R. Probing Single Molecules and Single Nanoparticles by Surface-Enhanced Raman Scattering. *Science* **1997**, *275*, 1102–1106.
53. Cançado, L. G.; Jorio, A.; Ismach, A.; Joselevich, E.; Hartschuh, A.; Novotny, L. Mechanism of Near-Field Raman Enhancement in One-Dimensional Systems. *Phys. Rev. Lett.* **2009**, *103*, 186101.
54. Novotny, L. The History of Near-Field Optics. *Prog. Opt.* **2007**, *50*, 137–184.
55. Kawata, S.; Inouye, Y.; Verma, P. Plasmonics for Near-Field Nano-imaging and Superlensing. *Nat. Photon.* **2009**, *3*, 388–394.
56. Kawata, S. ; Shalaev, V. M. (Eds.) *Tip Enhancement, Advances in Nano-Optics and Nano-Photonics*; Elsevier: Amsterdam, 2007.
57. Hartschuh, A.; Sanchez, E.; Xie, X.; Novotny, L. High-Resolution Near-Field Raman Microscopy of Single-Walled Carbon Nanotubes. *Phys. Rev. Lett.* **2003**, *90*, 095503.
58. Kunz, K. S.; Luebbers, R. J. *The Finite-Difference Time-Domain Methods*; CRC Press: Boca Raton, 1993.
59. Lidorikis, E.; Egusa, S.; Joannopoulos, J. D. Effective Medium Properties and Photonic Crystal Superstructures of Metallic Nanoparticle Arrays. *J. Appl. Phys.* **2007**, *101*, 054304.
60. Lidorikis, E.; Ferrari, A. C. Photonics with Multiwall Carbon Nanotube Arrays. *ACS Nano* **2009**, *3*, 1238–1248.
61. Chen, J. C.; Li, K. Quartic Perfectly Matched Layers for Dielectric Waveguides and Gratings. *Microwave Opt. Technol. Lett.* **1995**, *10*, 319–323.
62. Grigorenko, A. N.; Geim, A. K.; Gleeson, H. F.; Zhang, Y.; Firsov, A. A.; Khrushchev, I. Y.; Petrovic, J. Nanofabricated Media with Negative Permeability at Visible Frequencies. *Nature* **2005**, *438*, 335–338.
63. Grigorenko, A. N.; Roberts, N. W.; Dickinson, M. R.; Zhang, Y. Nanometric Optical Tweezers Based on Nanostructured Substrates. *Nat. Photon.* **2008**, *2*, 365–370.
64. Kravets, V. G.; Schedin, F.; Grigorenko, A. N. Plasmonic Blackbody: Almost Complete Absorption of Light in Nanostructured Metallic Coatings. *Phys. Rev. B* **2008**, *78*, 205405.
65. Kravets, V. G.; Grigorenko, A. N.; Nair, R. R.; Blake, P.; Anissimova, S.; Novoselov, K. S.; Geim, A. K. Spectroscopic Ellipsometry of Graphene and an Exciton-Shifted van Hove Peak in Absorption. *Phys. Rev. B* **2010**, *81*, 155413.
66. Palik, E. D. *Handbook of Optical Constants of Solids*; Academic: San Diego, CA, 1998.
67. Nair, R. R.; Blake, P.; Grigorenko, A. N.; Novoselov, K. S.; Booth, T. J.; Stauber, T.; Peres, N. M. R.; Geim, A. K. Fine Structure Constant Defines Visual Transparency of Graphene. *Science* **2008**, *320*, 1308.
68. Berciaud, S.; Ryu, S.; Brus, L. E.; Heinz, T. F. Probing the Intrinsic Properties of Exfoliated Graphene: Raman Spectroscopy of Free-Standing Monolayers. *Nano Lett.* **2009**, *9*, 346–352.
69. Link, S.; El-Sayed, M. A. Shape and Size Dependence of Radiative, Non-radiative and Photothermal Properties of Gold Nanocrystals. *Int. Rev. Phys. Chem.* **2000**, *19*, 409–453.
70. Lamprecht, B.; Schider, G.; Lechner, R. T.; Ditlbacher, H.; Krenn, J. R.; Leitner, A.; Aussenegg, F. R. Metal Nanoparticle Gratings: Influence of Dipolar Particle Interaction on the Plasmon Resonance. *Phys. Rev. Lett.* **2000**, *84*, 4721–4724.
71. Mie, G. Beiträge zur Optik Trüber Medien, Speziell Kolloidaler Metallösungen. *Ann. Phys.* **1908**, *25*, 377–445.
72. Bohren, C. F.; Huffman, D. R. *Absorption And Scattering Of Light By Small Particles*; Wiley: New York, 1983.
73. Basko, D. M.; Piscanec, S.; Ferrari, A. C. Electron−Electron Interactions and Doping Dependence of the Two-Phonon Raman Intensity in Graphene. *Phys. Rev. B* **2009**, *80*, 165413.
74. McCall, S. L.; Platzman, P. M.; Wolff, P. A. Surface Enhanced Raman Scattering. *Phys. Lett. A* **1980**, *77*, 381–383.
75. Thomsen, C.; Reich, S. Double Resonant Raman Scattering in Graphite. *Phys. Rev. Lett.* **2000**, *85*, 5214–5217.
76. Tuinstra, F.; Koenig, J. L. Raman Spectrum of Graphite. *J. Chem. Phys.* **1970**, *53*, 1126–1130.
77. Bonini, N.; Lazzeri, M.; Marzari, N.; Mauri, F. Phonon Anharmonicities in Graphite and Graphene. *Phys. Rev. Lett.* **2007**, *99*, 176802.
78. Lazzeri, M.; Piscanec, S.; Mauri, F.; Ferrari, A. C.; Robertson, J. Electron Transport and Hot Phonons in Carbon Nanotubes. *Phys. Rev. Lett.* **2005**, *95*, 236802.
79. Benedict, L. X.; Louie, S. G.; Cohen, M. L. Static Polarizabilities of Single-Wall Carbon Nanotubes. *Phys. Rev. B* **1995**, *52*, 8541–8549.
80. Kreibig, U.; Von Fragstein, C. The Limitation of Electron Mean Free Path in Small Silver Particles. *Z. Phys.* **1969**, *224*, 307–323.
81. Jackson, J. D. *Classical Electrodynamics*; Wiley: New York, 1999.
82. Kuzmenko, A. B.; van Heumen, E.; Carbone, F.; van der Marel, D. Universal Optical Conductance of Graphite. *Phys. Rev. Lett.* **2008**, *100*, 117401.
83. Ando, T.; Zheng, Y.; Suzuura, H. Dynamical Conductivity and Zero-Mode Anomaly in Honeycomb Lattices. *J. Phys. Soc. Jpn.* **2002**, *71*, 1318–1324.
84. Gusynin, V. P.; Sharapov, S. G.; Carbotte, J. P. Unusual Microwave Response of Dirac Quasiparticles in Graphene. *Phys. Rev. Lett.* **2006**, *96*, 256802.
85. Falkovsky, L. A.; Varlamov, A. A. Space−Time Dispersion of Graphene Conductivity. *Eur. Phys. J. B* **2007**, *56*, 281–284.
86. Wooten, F. *Optical Properties Of Solids*; Academic Press: New York, 1972.